

# Constraining the luminosity function of faint undetected $i$ -dropout galaxies<sup>1</sup>

V. Calvi<sup>2,3\*</sup>, A. Pizzella<sup>2,4</sup>, M. Stiavelli<sup>3</sup>, L. Morelli<sup>2,4</sup>, E. M. Corsini<sup>2,4</sup>, E. Dalla Bontà<sup>2,4</sup>, L. Bradley<sup>3</sup>, and A. M. Koekemoer<sup>3</sup>

<sup>1</sup> Based on observations with the NASA/ESA Hubble space telescope, obtained at the Space Telescope Science Institute, which is operated by the Association of Universities for Research in Astronomy, inc. under NASA contract NASS-26555

<sup>2</sup> Dipartimento di Fisica e Astronomia “G. Galilei”, Università di Padova, Vicolo dell’Osservatorio 3, I-35122 Padova, Italy.

<sup>3</sup> Space Telescope Science Institute, 3700 San Martin Drive, Baltimore, MD 21218, United States.

<sup>4</sup> INAF-Osservatorio Astronomico di Padova, Vicolo dell’Osservatorio 5, I-35122 Padova, Italy.

Accepted ... Received ...

## ABSTRACT

We present a new technique to quantify the light contribution coming from the faint high redshift ( $z \sim 6$ ) galaxies below the detection threshold of imaging data, set conventionally at  $S/N = 4.5$ . We illustrate the technique with an application to Hubble Space Telescope Advanced Camera for Surveys images in the F775W and F850LP filters of the Ultra Deep Field parallel field NICP12. The aim of this analysis is to extend by a few magnitudes the faint end of the luminosity function at  $z \sim 6$ . After masking all the detected sources in the field we apply a Fast Fourier Transform to obtain the spatial power spectrum of the background signal. The power spectrum permits us to separate the background noise signal, the residuals due to the data reduction of the wide field, and the overall signal produced by faint galaxies. The ratio of the signal in the  $i_{775}$  and  $z_{850}$  bands is used to estimate the contribution of the faint  $i$ -dropout objects. We rely on extensive Monte Carlo simulations to characterize various sources of uncertainty and quantify the number of faint  $i$ -dropout galaxies in the field. The analysis allows us to put constraints on the luminosity function at  $z \sim 6$  down to  $z_{850} = 30$  mag, 2.5 mag fainter than with standard techniques on the same data. The data are consistent with a faint end slope of the luminosity function of  $\alpha = -1.9$ . Assuming a specific set of values for the clumping factor, escape fraction, and spectral energy distribution, we find that the  $z \sim 6$  undetected galaxies down to  $z_{850} = 30$  mag could have driven cosmic reionization.

**Key words:** cosmology: early universe – galaxies: high-redshift

## 1 INTRODUCTION

In the last few years we have begun to investigate the cosmic reionization of hydrogen by using a variety of techniques. Reionization was completed between  $z \sim 10$  and  $z \sim 6$  (Loeb & Barkana 2001), bracketed by the detection of Gunn-Peterson troughs in the spectra of  $z \sim 6$  quasars (Fan et al. 2006) and by the Compton optical depth measured by the Wilkinson Microwave Anisotropy Probe (WMAP; Jarosik et al. 2011). However, the nature of the sources responsible for cosmic reionization is still an open question.

The UV photons expected to contribute to the reionization process come from mainly two sources, star forming galaxies and quasars. The former probably were fundamental for the hydrogen reionization, whereas the latter likely dominated the helium reionization (Shapiro & Giroux 1987; Madau et al. 1999). Accret-

ing black holes in the redshift range between  $z = 6$  and  $z = 8$  are rare and possibly obscured by significant amounts of gas and dust, so their UV emission probably does not contribute significantly to the reionization process (Treister et al. 2011). According to Fan et al. (2001), Meiksin (2005), and Shankar & Mathur (2007),  $z \sim 6$  quasars are not able to provide enough ionizing photons to contribute significantly to reionization.

Population III stars are also unlikely to dominate the ionizing UV production. In the standard scenario, in which only a single metal free star per dark halo is formed, the contribution to reionization given by Population III stars is only indirect. In fact, while the cumulative number of ionizing photons produced by them is not enough, they enrich the intergalactic medium of metals and allow the more efficient formation of following generations of Population II stars (Trenti & Stiavelli 2009). These stars are likely located in faint galaxies (Loeb & Barkana 2001).

A large optical depth to electron scattering, consistent with

\* E-mail: valentina.calvi.1@studenti.unipd.it

the Universe being reionized at  $z \sim 15$ , was found by WMAP (Bennett et al. 2003; Komatsu et al. 2011). Since there are still strong uncertainties on several key parameters concerning reionization, Kuhlen & Faucher-Giguère (2012) stated that it is not clear if galaxies could have completed the reionization by  $z \sim 6$  and account for the large optical depth to electron scattering found by WMAP-7. On the other hand, most of the studies carried out in the last decade are focused on the critical star formation rate density (SFRD). The Lyman break galaxies detected at  $z \sim 6$  (Stiavelli et al. 2004b) and  $z \sim 7$  (Bouwens et al. 2004; Bolton & Haehnelt 2007; Oesch et al. 2009) in the Hubble Ultra Deep Field (hereafter HUDF) are not bright enough to account for the required ionizing budget. However, more recently Finkelstein et al. (2012) have found that the detected galaxies at  $z \sim 6$  are sufficient to fully reionize the IGM if  $C/f_{esc} \sim 10$ . According to Bunker et al. (2010) and Finkelstein et al. (2010), the observed  $z \sim 7$  galaxies could have completed the reionization process if  $f_{esc} \geq 50\%$ . The observed faint-end slopes imply large numbers of undetected faint galaxies which likely provide the bulk of ionizing photons and played an important role in cosmic reionization (Yan & Windhorst 2004; Richard et al. 2008; McLure et al. 2010; Trenti et al. 2010; Bouwens et al. 2011).

Unfortunately, direct probing of the faint galaxy population is outside present capabilities and will need to wait for the James Webb Space Telescope (JWST). Thus, in order to make further progress in this field before the launch of JWST, one needs to find ways to study the faint end of the galaxy luminosity function at  $z \geq 6$  using the integrated light contribution of individually undetected galaxies. This idea is not new and it was tried in the context of high- $z$  studies using the Spitzer Infrared Array Camera (IRAC) and Advanced Camera for Surveys (ACS) data (Kashlinsky et al. 2007) and is, in fact, also analogous to the study of surface brightness fluctuations of nearby galaxies (Tonry & Schneider 1988).

The aim of this paper is to describe a new technique to analyze the contribution of faint, individually undetected, galaxies where we indicate as undetected galaxies those galaxies characterized by being fainter than the typical signal-to-noise ( $S/N$ ) ratio of 4.5 (Oesch et al. 2009). We focus mostly on galaxies just below the detection threshold as such galaxies are likely to exist, given that the luminosity function (LF) of galaxies should not know the HUDF magnitude limit, and they might be sufficient for reionization (Yan & Windhorst 2004).

These galaxies are too faint to be measured individually, but their signal can be quantified using a Fourier Transform based technique. The main difference here over the previous attempts at high redshift is our special attention to systematic effects.

The Lyman break technique permits to identify star-forming galaxies at high redshift using color criteria derived from a multi-band photometry in the region across the Lyman-continuum discontinuity (Steidel & Hamilton 1993; Giavalisco 1998). Comparing the flux of a galaxy within a set of two or three ad-hoc filters depending on the redshift, it can be noticed that no flux is collected by the bluer filter due to the Lyman  $\alpha$  absorption, while the object is detected in the redder bands.

In this paper we focus on  $i$ -dropout galaxies at  $z \sim 6$  that can be studied using images obtained with the same camera and characterized by, essentially, the same systematic effects. Galaxies at  $z \sim 6$  are expected to be undetected in the ACS F775W band (hereafter  $i_{775}$ ) image and detected in the ACS F850LP (hereafter  $z_{850}$ ) one, so they are named  $i_{775}$ -dropout galaxies.

The faint galaxy population we seek is detected by an excess

**Table 1.** Properties of the NICP12 data.

Filter	<i>HST</i> orbits <sup>a</sup>	Exposure Time <sup>a</sup> [s]	Zero Point <sup>b</sup> [AB mag]	10 $\sigma$ Magnitude <sup>a</sup> [AB mag]
$i_{775}$	23	54,000	25.654	28.44
$z_{850}$	69	168,000	24.862	28.47

<sup>a</sup> From Oesch et al. (2007)

<sup>b</sup> From de Marchi et al. (2004)

NOTES: Col. 1: filter name. Col. 2: number of HST orbits. Col. 3: total exposure time in seconds. Col. 4: zero point in AB magnitude. Col 5: 10  $\sigma$  limiting magnitudes in AB magnitude computed within apertures of 0.15'' radius.

in the power spectrum in the  $z_{850}$  image with respect to that of the  $i_{775}$  one, i.e., it is a Lyman break population.

In Section 2, we describe the data used. In Section 3, we explain the data analysis and we present the main steps of the power spectrum technique adopted to obtain the signal coming from the undetected galaxies, which are bona fide  $z \sim 6$  candidates. In Section 4, we describe how to estimate the contribution to cosmic reionization using Monte Carlo simulations, we discuss our results and their implications for the reionization epoch.

## 2 DATA SET

To date, the deepest optical data available are from the HUDF project (Beckwith et al. 2006) and the Hubble Ultra Deep Field Follow-Up (hereafter UDF05; Oesch et al. 2007). These ultra deep observations of multiple fields have been obtained with ACS. In this first application of our technique we selected the parallel field NICP12 rather than the main HUDF field. The reason for this is that the NICP12 images were produced with a more advanced data reduction than the one used in the main field (Oesch et al. 2007). In particular, an herringbone effect introduced inadvertently by the subtraction of a combined, high  $S/N$ , bias frame (superbias) made from compressed bias frames containing a small electronic noise component was eliminated as well as electronic ghost images of the bright sources. Thus, the improved version of the NICP12 images (v2.0) is the cleanest available. We are currently reprocessing the main HUDF field so as to bring it to the same standard and when this field will be available we plan to apply this analysis to it as well.

The coordinates of the center of the NICP12 field are R.A.=03<sup>h</sup>33<sup>m</sup>03.60<sup>s</sup>, Dec.=−27°41'01.80'' (J2000.0). The characteristics of the observations for the  $i_{775}$  and  $z_{850}$  images are specified in Table 2. Throughout this paper we used the AB mag magnitude system. The original images are characterized by a pixel scale of 30 mas pixel<sup>−1</sup> and a side of 10500 pixels. They were rotated to have North up and East left.

## 3 DATA ANALYSIS

A first step to reveal the contribution of undetected galaxies was to mask all the light coming from stars and detected galaxies, including their bright halos. Once the appropriate mask had been created we applied the power spectrum technique to analyze the different contributions existing in the background.

### 3.1 Creation of the Mask

Since the MULTIDRIZZLE task (Koekemoer et al. 2002) works on dithered observations of the same field and only a few pointings in the outer regions of the field can be combined, we used the weight maps associated to the v2.0 data to select the central region for the following analysis. The data we focused on were binned to have a scale of 90 mas pixel<sup>-1</sup> and a size of 3500 × 3500 pixels. This rebinning is intended to limit the computational volume, but it does not affect the final result, as discussed in Section 3.4.

First of all, we had to remove all the defects and objects that could interfere with our analysis, such as the detected galaxies, their bright halos, residual cosmic rays, and bad pixels. Galaxies were detected independently in the  $i_{775}$  and  $z_{850}$  images using the SExtractor photometry package by Bertin & Arnouts (1996), version 2.5.0. The SExtractor parameters were optimized to maximize the number of detected galaxies while minimizing the number of spurious sources. The detection threshold (DETECT\_MINAREA) was set to be a minimum of 5 connected pixels with an intensity of  $0.55\sigma$  (DETECT\_THRESH) above the background (Oesch et al. 2007).

Oesch et al. (2009) considered only those galaxies detected with  $S/N > 4.5$  to be reliable. Since we were interested in galaxies which are too faint to be individually studied, but that produce a relevant overall light contribution, we had to mask all the reliable single galaxies and focus on the total contribution of the fainter ones. We noted that, by doing this, we were sensitive to both galaxies just below our detection threshold and much fainter ones. This was intentional, as we were trying to constrain all contributions below those of reliably detected galaxies.

Starting from the segmentation maps, one of the outputs of SExtractor, we created two masks (one for each band) to reject all the detected sources existing in the field of view. Since most of the objects are surrounded by a bright halo, we decided to enlarge the masked area to avoid contaminating signal from bright galaxies. We reversed each mask to be 1 where there are sources and 0 elsewhere, we convolved two times the mask with a Gaussian filter with FWHM = 30 pixel = 2''.7 enlarging it each time by adding all the pixels with a value  $> 0.5$ . Finally we reversed again the mask. In this way we added  $\sim 18 - 19\%$  more pixels to the mask.

We obtained the final mask by merging the masks in the two passbands and convolving again. The masked area corresponds to 16.8% of the field.

### 3.2 The Power Spectrum Technique

A description of random fluctuations is fundamental to extract information hidden in the background of images and to provide a quantitative measure for the comparison with simulations. The spatial power spectrum is the key of our method, allowing us to determine the amplitude of surface brightness fluctuations and to distinguish the sources of noise from the fluctuations due to the unresolved galaxies. The power spectrum we mention is not the same applied first by Harrison (1970) and Zeldovich (1972), and then by White (1994) to study the cosmic microwave background (CMB) anisotropies. We are, instead, interested in the spatial distribution of the faint  $z \sim 6$  galaxies, so as to be able to extend the faint end of the luminosity function. For this reason we used the Fourier transform to derive the spatial power spectrum of the luminosity fluctuation due to these galaxies, similar to the work of Tonry & Schneider (1988) and Tonry et al. (1990). Using this method we are able to

constrain the number of the faint galaxies (see, however, comments at the end of Section 3.3).

A technique similar to ours was used for the first time by Tonry & Schneider (1988). They discovered that the distance of a galaxy is inversely proportional to the amplitude of the luminosity fluctuations due to unresolved red giant stars and they used the spatial power spectrum to directly measure these fluctuations. The main difference between their work and ours is the density of sources per pixel. They were studying nearby galaxies that have a projected density of stars of many tens per pixel so the fluctuations between adjacent pixels have rms variations  $\lesssim 10\%$  of the mean signal. On the contrary, we are dealing with images where the projected density of faint galaxies is much less than one per pixel, therefore we have smaller fluctuations and our results are more sensitive to the presence of spurious signals.

Our approach consists in applying the IDL<sup>1</sup> Fast Fourier Transform (FFT) routine to the masked images to compute the two-dimensional Fourier transform and, then, to derive the spatial power spectrum of the signal. Therefore, the power spectrum image obtained is two-dimensional, but to plot it and to do all the calculations in the following it is convenient to derive the radial trend.

The power spectra for the two bands can be compared by calculating their difference or ratio. The difference is the most natural choice, but relies on an extremely accurate color calibration of the power spectra in order to properly subtract the contribution of lower redshift objects from the  $z_{850}$  power spectrum. The ratio allows us to avoid the need of a very accurate and challenging color calibration of the power spectra. Thus, from here on, we focus our analysis on the ratio of power spectra.

We obtained the power spectra for both the  $i_{775}$  and  $z_{850}$  images (Figure 1). To highlight the light contribution coming from the undetected galaxies, which are bona fide  $z \sim 6$  candidates, we examined the ratio between the  $z_{850}$  and  $i_{775}$  power spectra (Figure 2). These undetected galaxies are responsible for a peak located between wavenumbers,  $k$ , of 100 and 400, shown in Figure 2. We tested the reliability of this feature using a  $\chi^2$  statistics. Comparing the values of the ratio between the power spectra in the range of the peak, i.e.  $100 \lesssim k \lesssim 400$ , and in the range  $1400 \lesssim k \lesssim 1700$  dominated only by the noise, we obtained  $\chi^2_\nu = 3.08$ . This value, which can be rejected with a confidence well beyond  $10\sigma$ , convinced us that the peak is a real feature and it can not be ascribed to random noise.

The angular scale  $\theta$ , plotted on the top x-axis of the figures, is derived from  $k$  as follows:

$$\theta [\text{arcsec}] = \frac{D_{\text{frame}} [\text{pixel}] \cdot \text{scale} [\text{arcsec pixel}^{-1}]}{k} \quad (1)$$

where  $D_{\text{frame}}$  is the dimension of the frame in pixels and scale is the pixel scale of the image.

Following our technique, we can derive the number of faint galaxies from the height of the signal excess they produce in the ratio between the power spectra (Figure 2) and by comparing it with the one obtained from simulations (see Section 4).

It must be noted that our result can be affected by a fraction of interlopers at lower redshift. This is an issue affecting all studies based on the dropout selection and it is due to the aliasing between the Lyman break and the 4000 Å break, as discussed by Dahlen et al. (2010). Su et al. (2011), on the basis of accurate simulations, estimated that the fraction of  $z \sim 1.2$  galaxies which can

<sup>1</sup> Interactive Data Language is distributed by Exelis Visual Information Solutions.

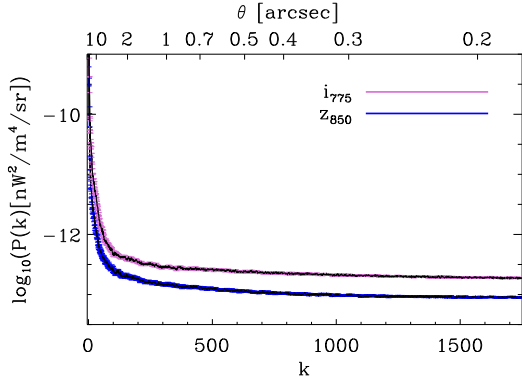


**Figure 1.** Power spectra, with colored error bars, of the background signal of the  $i_{775}$  (top line with purple error bars) and  $z_{850}$  images (bottom line with blue error bars).

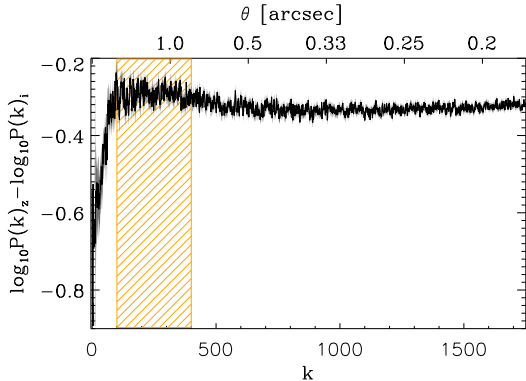


**Figure 2.** Ratio between the  $z_{850}$  and  $i_{775}$  power spectra. The shaded grey area represents the errors associated to the ratio. The region between  $k = 100$  and  $k = 400$ , where the signal from the faint galaxies was measured, is highlighted in orange.

be selected as  $z \sim 6$  population could be as high as 24%. This value is a pessimistic one since Malhotra et al. (2005) found half that number of contaminant galaxies, based on ACS grism observations.

### 3.3 Different Contributions

The use of the power spectrum technique requires a preparatory study to understand how the different components of a scientific image affect the final power spectrum.

The ratio between the spatial power spectra in Figure 2 can be divided into three different parts, the first one at low wave numbers ( $k \lesssim 100$ ), the second one in the range of high wave numbers ( $k \gtrsim 400$ ) and the remaining one at intermediate wave numbers, which corresponds to the contribution from the undetected galaxies at  $z \sim 6$ .

The power spectrum of random noise is a white power spectrum having approximately a constant value over all the range of wave numbers. At high wave numbers, meaning at the pixel scale, the white noise contribution is dominant. At low wave numbers the principal contribution is due to residuals of the flat field correction

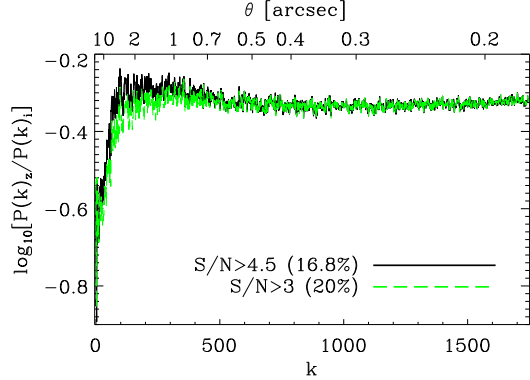


**Figure 3.** Ratios between the  $z_{850}$  and  $i_{775}$  power spectra obtained masking all the sources detected by SExtractor with  $S/N > 4.5$  (black line) and  $S/N > 3$  (green dashed line). The percentages indicate the masked area.

process (for more details on this see Section 3.4). The highlighted region of the plot in Figure 2 is the most interesting one, where the signal is dominated by the contribution of the galaxies, therefore it permits us to infer the existence of galaxies below the usual detection limit. In particular, the amplitude of the peak visible between  $k = 100$  and  $k = 400$  is proportional to the number of undetected galaxies in the field.

### 3.4 Possible Sources of Contamination

There are many sources of uncertainties that can affect our results and we will briefly list and characterize them.

**Mask:** The primary source of uncertainty in our results is the size of the mask. Our aim is to mask all the galaxies which can be reliably and individually identified and to study the overall signal coming from those which are too faint to be detected one by one. If we are masking to a signal level which is too low, we will not see any signal coming from faint galaxies. On the other hand, if the mask brightness limit is too high the faint  $z \sim 6$  undetected galaxies will be overwhelmed by the light of the foreground galaxies and their bright halos. The ratio between the power spectra obtained by masking all the sources detected by SExtractor with  $S/N > 4.5$  and  $S/N > 3$  are compared in Figure 3. In the region between  $k = 100$  and  $k = 400$  we notice that the peak due to the signal of faint  $i$ -dropouts is significantly lower and almost invisible. As the percentage of masked area is quite similar (16.8% and 20%), we can infer that we are detecting a signal from galaxies barely below our detection threshold rather than from a multitude of very faint objects.

**Calibration Files and Dither Pattern:** The use of MultiDrizzle could introduce spurious signals in the final scientific frame obtained after the combination of all the  $flt$  files. To test this, we downloaded all the  $flt$  data available for the NICP12 field in the  $i_{775}$  and  $z_{850}$  bands from the HST archive and replaced the scientific frame with random noise. The resulting mock frames have no sources and maintain the same coordinates of the real ones. Then, for each filter we processed these noise-only frames with MultiDrizzle, and we applied the power spectrum technique to the final scientific images. As it can be noticed from Figure 4 no features are introduced by MultiDrizzle neither in the single power spectra (top panel), nor in the ratio (bottom panel). Moreover, we did a similar test combining mock frames with noise multiplied by a random residual of flat field

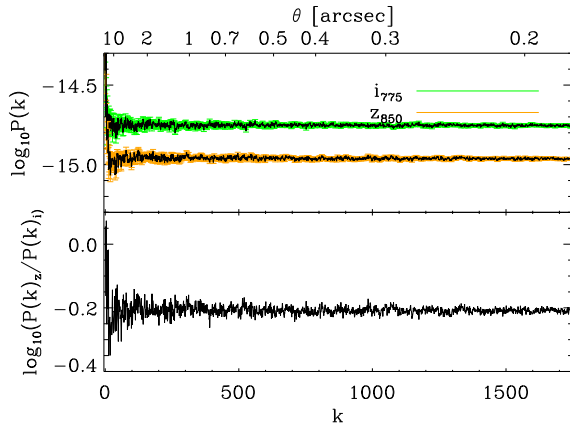


**Figure 4.** Power spectra derived by combining the noise-only frames with MultiDrizzle (top panel) and their ratio (bottom panel). The flatness of the profile indicates that no features were introduced when combining the images with MultiDrizzle.

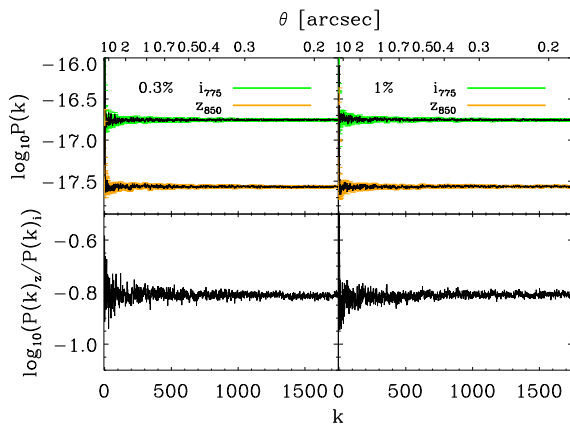


**Figure 5.** Power spectra derived by combining with MultiDrizzle noise-only frames after being multiplied by a random residual of flat field with a maximum of 0.3% (top left panel) and 1% (top right panel) and their ratio (bottom panel). As in Figure 4, no spurious feature is introduced in the final ratio when combining the images with MultiDrizzle.

(with a maximum of 0.3% and 1%) and, then, applying the power spectrum technique. It should be noted that the flat field residual in this case introduces a pixel-to-pixel uncertainty, not a large scale one. Once again, we concluded that MultiDrizzle is not creating spurious signals (see Figure 5) and, consequently, it is not affecting the final result of our technique.

**Cosmic Ray Residuals:** The presence of cosmic ray residuals in the frame results in a gentle increasing slope in the range of high wave numbers, which depends on the intensity and number of pixels affected by the cosmic rays.

**Zodiacal Light:** The zodiacal light is the dominant source of sky brightness in the near-IR (Reach 1997). We were only interested in the fluctuations due to the zodiacal light cloud changing in the sky during the time of the observations. According to Kashlinsky et al. (2005), considering two observations of the same field taken six months apart and computing their difference, it is possible to isolate the zodiacal light fluctuation from the contribution coming from galactic and extragalactic objects. With this method Kashlinsky et al. (2005) were able to derive an upper limit

for the zodiacal light contribution and to affirm that it did not affect their results on the cosmic infrared background fluctuations. Unfortunately, a few issues prevented us from applying the same analysis to the HST data. First of all, observations taken six months apart imply different orientations of the camera which could introduce detector-related systematics leaving a signature in the power spectrum. Moreover, ACS is affected by the contribution of scattered sunlight whenever the angle is close to (or less than)  $90^\circ$  and this could determine a wrong estimate of the fluctuation ascribable to zodiacal light. Finally, at the moment we do not have observations of our fields taken with such a long temporal delay, so we cannot study relevant zodiacal fluctuations. On the basis of above, we decided to assume a negligible zodiacal contribution following Kashlinsky et al. (2005) and to better handle the zodiacal light fluctuation in our next paper, analyzing observations of the same field obtained with a long temporal separation, so as to highlight relevant differences in the zodiacal light.

**Flat Field Correction and Bias Subtraction Residuals:** If the flat field correction or bias subtraction process were not correctly done, the data could be affected by a diffuse signal not coming from any real source. It can easily overcome the small amount of photons produced by the undetected galaxies we are looking for. These residuals modify the trend of each single power spectrum, increasing its slope in the low and medium wave numbers ranges and making difficult to see any peak in the power spectra ratio.

**Rotation:** The images we used, oriented with North up and East left, were obtained from MULTIDRIZZLE without introducing any additional correlation between adjacent pixels (Casertano et al. 2000) because of the use of the point kernel (Beckwith et al. 2006). We did not introduce any further rotation in our data, nevertheless, we decided to investigate this effect for sake of completeness since this is a technical paper describing all the aspects of our new technique. If we were dealing with rotated frames it would be important to consider the following effect. The rotation of the images before extracting the power spectrum determines a correlation between adjacent pixels, which is detected as a clear slope at high wave numbers of both the  $i_{775}$  and  $z_{850}$  power spectra (Figure 6). The magnified panel shows that the power spectra of the original and rotated data present different slopes, but, as shown in Figure 7, the ratio of the power spectra is not significantly affected by rotation since the slope introduced is exactly the same in both the  $i_{775}$  and  $z_{850}$  power spectra. The ratio of the rotated data fits extremely well with that of the unrotated ones.

**Binning:** To test the effect of data binning we compared the results obtained from the images with a pixel scale of  $90 \text{ mas pixel}^{-1}$  and a dimension of 3500 pixel each side, and the original images, characterized by a pixel scale of  $30 \text{ mas pixel}^{-1}$  and a 10500 pixel side. By binning the data, we lost details and so the power spectrum covers a more limited range of wave numbers. However, the ratio between the power spectra plotted in Figure 8 shows that the white power spectrum is well reproduced by both the  $30 \text{ mas pixel}^{-1}$  and the  $90 \text{ mas pixel}^{-1}$  cases.

**Groups of Galaxies:** It is known that galaxies at high redshift are not necessarily randomly distributed, but can be grouped. Overzier et al. (2006) studied the clustering properties of galaxies at  $z \sim 6$  finding an angular correlation for galaxies brighter than  $z_{850}=28.5$  mag on scales larger than  $10''$  and no correlation on the same scales going down to  $z_{850}=29.0$  mag due to low S/N. Studying a sample of galaxies at  $z \sim 5$ , Lee et al. (2006) found a further correlation on smaller angular scales, which was interpreted as due to the so-called one-halo term. The clustering properties, due to both the one-halo and the two-halo term, are still not well

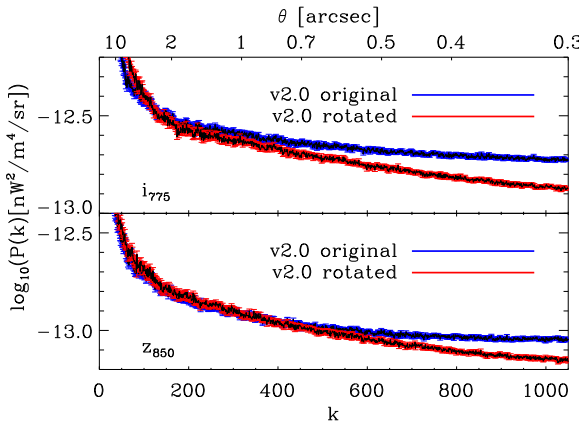


**Figure 6.** Power spectra obtained from the  $i_{775}$  (top panel) and  $z_{850}$  (bottom panel) images with (bottom line with red error bars) and without (top line with blue error bars) applying a  $45^\circ$  clockwise rotation. In each panel the power spectrum referring to the rotation was vertically shifted to match the other one at  $k = 125$  ( $D_{\text{galaxies}} = 2''.52$ ) to better show the effect of the rotation.

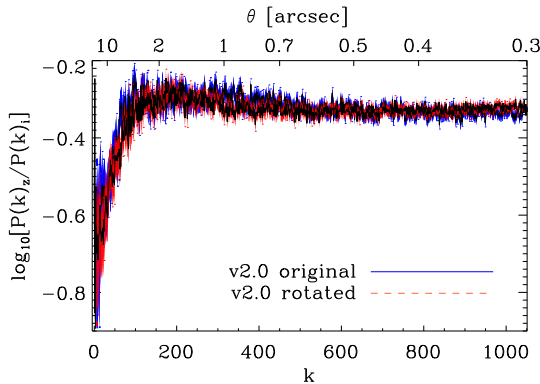


**Figure 7.** Comparison of the ratios between the  $z_{850}$  and  $i_{775}$  power spectra for the v2.0 data with (red dashed error bars) and without (blue solid error bars) applying a  $45^\circ$  clockwise rotation. The rotation has no significant effect on the ratio.

explored for  $i_{775}$ -dropouts with magnitudes in the range between  $z_{850}=28$  mag and  $z_{850}=30$  mag. Moreover, our field is too small to be affected by the large angular scale clustering which is better constrained (Overzier et al. 2006) than the small scale one. On the basis of this, we explored the effect of galaxy grouping on the power spectrum building up a toy model which introduces pairs of sources instead of randomly distributing them according to a non-zero angular correlation function only on scales smaller than  $10''$ .

We assumed the one-halo term of  $\omega(\theta)$  found by Lee et al. (2006) for  $V_{606}$ -dropout galaxies to be valid also for  $i_{775}$ -dropouts and placed the mock galaxies in the simulated frame accordingly. We found that clustering could amplify the signal from faint galaxies. In particular, simulations with no clustering leads to an overestimation of number of faint galaxies (see Section 4 for more details). In any case, since the clustering/grouping properties of  $i_{775}$ -dropouts on the smaller angular scales are not known at the present epoch, our findings need to be revisited as soon as a proper angular correlation function is found at  $z \sim 6$ .

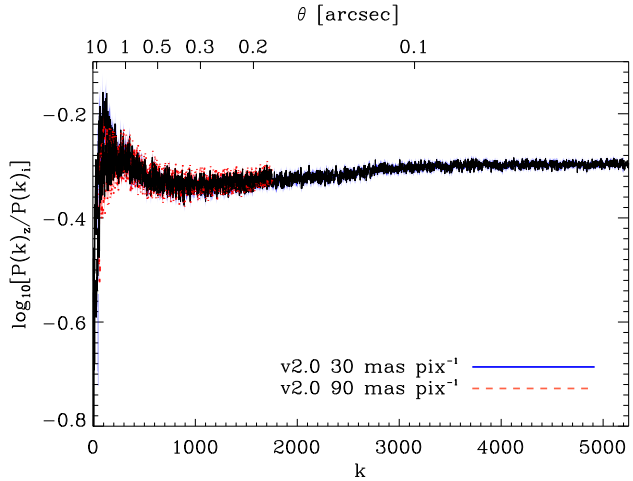


**Figure 8.** Ratios between the  $z_{850}$  and  $i_{775}$  power spectra obtained for the v2.0 images with a pixel scale of 30 (blue solid line error bars) and 90 mas pixel $^{-1}$  (red dashed line error bars). By binning the data the power spectrum covers a smaller wave number range, but the different pixel scale is not affecting the features we are interested in.

#### 4 MONTE CARLO SIMULATIONS

The power spectrum permits us to see the existence of an overall signal coming from faint galaxies, but we are not able to directly obtain neither the number of those galaxies nor their magnitudes. To derive the number and properties of the undetected galaxies responsible for the signal detected in the FFT we performed a series of Monte Carlo simulations.

To create the mock  $i_{775}$  and  $z_{850}$  images of the NICP12 field we started by deriving the values of the magnitudes, below the detection limit, and the morphology to assign to the simulated galaxies. Then, we focused on the way to resemble as well as possible the noise and the large scale effects characteristic of the data. Finally, we compared the power spectra obtained from the ACS data with the results coming from the simulations. We iterated the simulation 100 times to estimate the variability of the power spectra depending on the elements we used.

##### 4.1 Elements of the Simulations

In the following all the elements used in the simulations will be fully discussed.

*Random Noise:* We used the IDL RANDOMN routine to create a frame with the same size of our images and randomly distributed values with a mean of zero and a standard deviation of one. Subsequently, to reproduce the typical noise of the ACS data, we multiplied this frame by the characteristic standard deviation of the  $i_{775}$  and  $z_{850}$  images we measured with the IRAF<sup>2</sup> task IMSTATISTICS. The resulting two random noise frames have a white power spectrum and reproduce exactly the trend observed at high wave numbers in Figure 1.

*Large Scale Effects:* The residuals of the flat field correction produce the peak at low wave numbers in both the  $i_{775}$  and  $z_{850}$

<sup>2</sup> Imaging Reduction and Analysis Facilities (IRAF) is distributed by the National Optical Astronomy Observatories which are operated by the Association of Universities for Research in Astronomy (AURA) under cooperative agreement with the National Science Foundation.

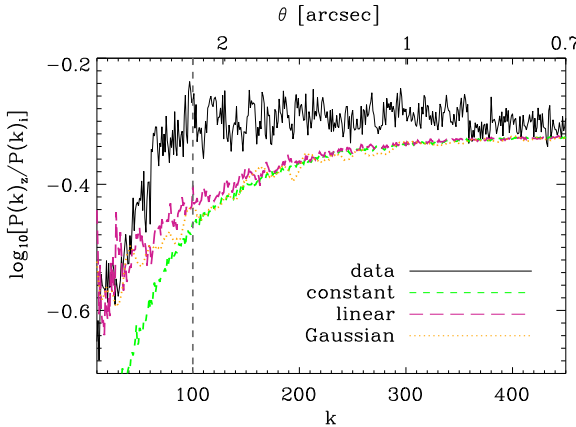


**Figure 9.** Comparison of the ratios between the  $z_{850}$  and  $i_{775}$  power spectra obtained from simulations including only noise and large scale residuals. Different models of large scale residuals were tested: a constant (green short dashed line), a linear one (magenta long dashed line), and a Gaussian one (orange dotted line). In black is plotted the ratio between the power spectra derived from the data. The dashed vertical line indicates the limit of the wave numbers range affected by the type of model considered for the large scale residuals.

power spectra (Figure 1). Since we were not interested in studying the trend in the low wave number range, we simply searched a way to recover the shape of the power spectrum in this range. We created a model of flat field residuals to reproduce the large scale effects and, then, we added it to the simulated frame (additive flat field residuals). To be sure our model was not affecting the results of the simulations, we performed tests using mock frames with only noise and large scale residuals, assuming different models for the latter. In particular, we considered a Gaussian model, a uniform model (i.e. a constant flat), and one with a linear slope. As can be seen in Figure 9 the differences in the results are confined in the very low wave number range ( $k < 100$ ), up to the dashed vertical line and it is not possible to reproduce the signal excess due to faint galaxies with only noise and flat field residuals. On the basis of these results we can affirm that the adopted model is not affecting the range we are interested in, and the signal in  $100 < k < 400$  is not affected by our choice regarding the modeling of the residuals of the flat field correction.

*Faint Galaxies:* To determine the magnitudes of the simulated faint galaxies, we considered all the detected galaxies of the field. The histogram of the distribution of the values of the total magnitude (obtained from the MAG\_AUTO parameter in SExtractor) for the  $i_{775}$  image is shown in the top panel of Figure 10. The value of 28.5 mag, where the number of galaxies decreases by a factor larger than 50%, is assumed as the brighter limit for the range of magnitudes used in the simulation of the  $i_{775}$  image. The fainter limit is  $i_{775} = 30.5$  mag, as we will see later in this Section.

The number of faint galaxies with  $z \leq 5$  to be inserted in the mock  $i_{775}$  image was derived extrapolating the trend of the number counts beyond the cut off assuming a slope  $\alpha_i = -1.3$  according to Metcalfe et al. (1995). The number of galaxies for each bin of magnitude used in the simulation is specified in Table 2.

To reproduce the  $z_{850}$  image, we considered both the  $z \sim 6$  faint galaxies and those at  $z \leq 5$ . The latter include the same mock galaxies used to simulate the  $i_{775}$  image, whose magnitudes were corrected with a color term randomly drawn from a distribution reproducing the  $i_{775}-z_{850}$  color observed for the detected galaxies.

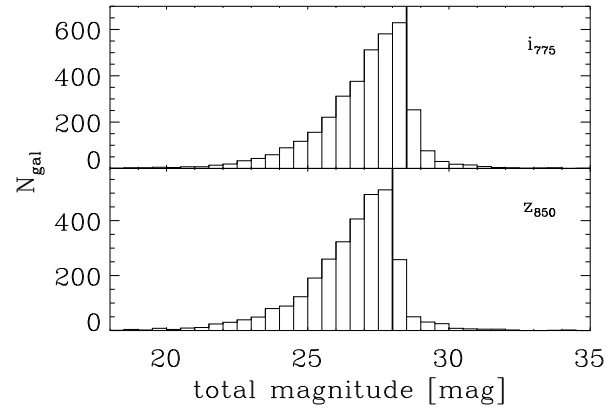


**Figure 10.** Distribution of the total magnitude of the detected galaxies in the  $i_{775}$  (top panel) and  $z_{850}$  (bottom panel) images. The vertical line corresponds to the magnitude where we observe a drop in the galaxy number and which was assumed as the brightest magnitude used in our simulations.

**Table 2.** Number and magnitudes of the simulated galaxies.

$z \leq 5, \alpha_i = -1.3$		$z = 6, \alpha = -1.9$	
Mag	Number	Mag	Number
28.5	714	28.0	32
29.0	1605	28.5	87
29.5	3008	29.0	233
30.0	5503	29.5	622
30.5	10028	30.0	1665

The former population consists of  $z \sim 6$  galaxies not detectable in the  $i_{775}$  image. The brighter limit for the magnitude range is assumed to be the value of 28 mag where the histogram of the total magnitudes shows a drop larger than 50% (Figure 10, bottom panel). The fainter limit of the range considered is  $z_{850} = 30.5$  mag. We extrapolated to fainter magnitudes the luminosity function at  $z \sim 6$  to obtain the number of galaxies to be created.

All the simulations hereafter include a flat field residual model. After a series of tests, we found a good agreement in reproducing this effect by combining 20 Gaussian functions with a standard deviation of about one third of the image dimension: 10 of them have a peak of  $10^{-4}$  to match the typical fluctuations of the flat field, and the other 10 Gaussians have a peak of  $-10^{-4}$  to create a smooth background with soft large scale fluctuations. The chi-square statistics results obtained comparing the data to the simulations including the three different flat-field models plus mock galaxies and noise in the range  $100 < k < 400$  were very similar (see Columns 3 and 4 in Table 3 and panel (b) of Figure 16).

We tested different values for the slope  $\alpha$ , in particular  $\alpha = -1.3, \alpha = -1.7, \alpha = -1.9, \alpha = -2.1$ , and  $\alpha = -2.4$ . On the basis of a  $\chi^2$  statistics (see columns 7 and 8 of Table 3 and (b) panel of Figure 16) we assumed our extrapolation to have the slope  $\alpha = -1.9$  (Figure 11) and we anchored it to the LF value at a magnitude of 28 mag given by Bouwens et al. (2007). This value is in agreement with the expectation of Su et al. (2011), who found the faint end slope of the LF at  $z \sim 6$  to be in the range  $-1.90 < \alpha < -1.55$ .

Testing the effect of groups of galaxies as described in Section

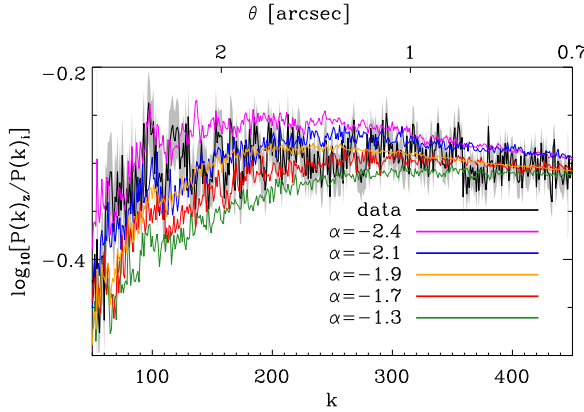


**Figure 11.** Comparison of the ratio between the simulated power spectra derived assuming different faint end slopes. The green, red, orange, blue, and magenta lines represent the median obtained from simulations assuming  $\alpha = -1.3$ ,  $\alpha = -1.7$ ,  $\alpha = -1.9$ ,  $\alpha = -2.1$ , and  $\alpha = -2.4$ , respectively. In black the ratio derived from the data is plotted with its error bars.

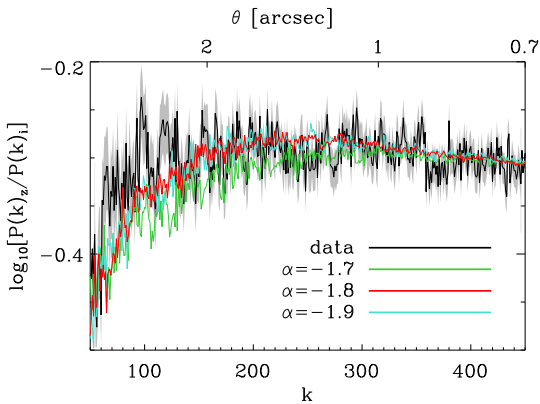


**Figure 12.** Comparison of the ratio between the simulated power spectra derived assuming different faint end slopes and pairs of galaxies with a distance derived from the angular correlation function at  $z \sim 5$  (Lee et al. 2006). The green, red, and blue lines represent the median obtained from simulations assuming  $\alpha = -1.7$ ,  $\alpha = -1.8$ , and  $\alpha = -1.9$ , respectively. In black the ratio derived from the data is plotted with its error bars.

3.4, we considered different slopes  $\alpha$ , i.e.  $\alpha = -1.7$ ,  $\alpha = -1.8$ , and  $\alpha = -1.9$  introducing pairs of mock galaxies in the simulation (Figure 12). The  $\chi^2$  statistics shows that  $\alpha = -1.8$  fits best the data ( $\chi^2_\nu = 1.06$ , see Columns 9 and 10 of Table 3).

Finally we also considered the effect of contaminants at lower redshift changing the low-luminosity slope of the distribution of galaxies with  $z \leq 5$ . To this aim we considered higher and lower values for  $\alpha_i$  and we noted that this change produces a similar one, with opposite sign, in the derived  $\alpha$  value at  $z \sim 6$ .

In building the set of galaxies, we considered a range of geometrical (i.e., position and orientation on the frame) and structural parameters (i.e., effective radius,  $r_e$ , and axis ratio,  $b/a$ ). Each synthetic galaxy was generated with a set of random, equally distributed, values for the former parameters and a set of values which resembles the characteristics of the fainter detected galaxies of the NICP12 field, derived from the catalog obtained running SExtractor, for the latter. Regarding the former parameters, each synthetic

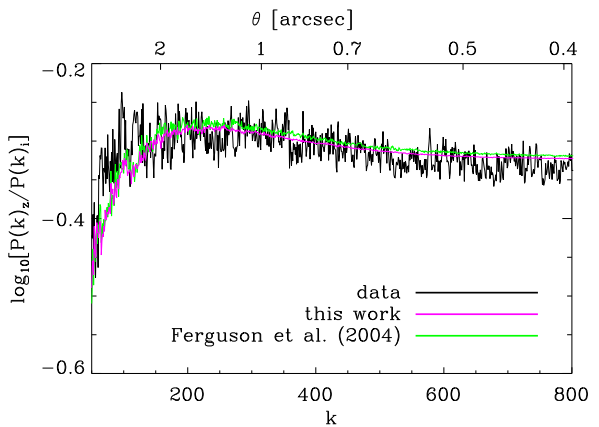


**Figure 13.** Comparison between the ratio of the power spectra obtained from the data (black line) and from the simulations assuming our effective radius distribution (magenta line) and the one by Ferguson et al. (2004, green line)

galaxy was generated with a set of random values. On the other hand, the structural parameters values had to resemble the characteristics of the fainter detected galaxies of the NICP12 field, derived running SExtractor. The values of the effective radius were chosen within the range  $1.5 \leq r_e \leq 11$  pixel corresponding to  $0''.135 \leq r_e \leq 0''.99$ , and the range spanned by the axis ratio was  $0.3 \leq b/a \leq 1$ . Even though the distribution of  $r_e$  we used was only slightly different from the one found by Ferguson et al. (2004) at  $z \sim 5$ , we tested the effect of this parameter on the simulations (Figure 13). In particular, the reduced chi-square statistics ( $\chi^2_\nu = 1.22$ ) supports the idea that small differences in the  $r_e$  distribution do not significantly affect the result.

Finally, we convolved the mock galaxies with the HUDF PSF (FWHM  $\sim 0''.1$ , Oesch et al. 2007).

*Galaxy Morphology:* Regarding the morphology of the mock galaxies, we adopted a Sérsic profile and, changing the Sérsic index  $n$ , we obtained ellipticals ( $n = 4$ ) and spirals ( $n = 1$ ). Since there are no clear indications regarding the distribution of different galactic types in the early Universe, we studied the effect of changing the relative number of ellipticals and spirals in our simulations. We compared the results obtained introducing 15% ellipticals (described by a de Vaucouleurs profile) and consequently 85% spirals (described by an exponential profile) in the simulations with those obtained simulating 50% ellipticals and 50% spirals and 33% ellipticals and 67% spirals. In Figure 14 the ratio of the power spectra obtained from the data is compared with the mean ratios and  $3\sigma$  confidence ranges derived from simulations with different distributions of ellipticals and spirals. Applying the chi-square statistics to the wave number range where the peak is, i.e.  $100 \lesssim k \lesssim 400$  (see Columns 1 and 2 in Table 3) we selected the realization characterized by the smallest  $\chi^2$  value as the best fit (see also the distribution of the residuals in the (a) panel of Figure 16). It corresponds to the mix of 33% ellipticals and 67% spirals. These percentages are consistent with the findings of Somerville et al. (2001), who predicted the majority of galaxies at  $z \geq 3$  to be disk dominated, and of Lotz et al. (2006) and Ravindranath et al. (2006) who found the percentage of galaxies with bulgelike morphology to be  $\sim 30\%$  at  $z \sim 3$  and  $z \sim 4$ , respectively.

This mix was adopted to test the sensitivity of the method to the assumed value of the faint end limit. To this aim we performed a few simulations changing the fainter magnitude limit of the mock

**Table 3.** The results obtained from the  $\chi^2$  statistics are listed for all the realizations of the simulations regarding the percentage of elliptical and spiral galaxies (Columns 1 and 2), flat field residual model (Columns 3 and 4) introduced, value of the cut-off in magnitude (Columns 5 and 6), and slope of the faint end of the LF with single sources (Columns 7 and 8) and with pairs of galaxies (Columns 9 and 10), respectively. The selected realization is the one characterized by the smallest  $\chi^2_\nu$  value, i.e.  $\chi^2_\nu = 1.02$ . A value of  $\chi^2_\nu = 1.24$  corresponds to a probability of 0.3% and it can be rejected with a  $3\sigma$  confidence level.

Percentage of E and S	Flat field residual model		Magnitude cut-off		Faint end slope $\alpha$		Grouping slope $\alpha$	
	sim	$\chi^2_\nu$	sim	$\chi^2_\nu$	sim	$\chi^2_\nu$	sim	$\chi^2_\nu$
15% E	1.47	Gaussian	1.02	29.5 mag	1.60	$\alpha = -1.3$	3.22	$\alpha = -1.7$
33% E	1.02	linear	1.04	30.0 mag	1.70	$\alpha = -1.7$	1.65	$\alpha = -1.8$
50% E	1.49	constant	1.04	30.5 mag	1.02	$\alpha = -1.9$	1.02	$\alpha = -1.9$
				31.0 mag	1.33	$\alpha = -2.1$	1.47	
						$\alpha = -2.4$	2.53	

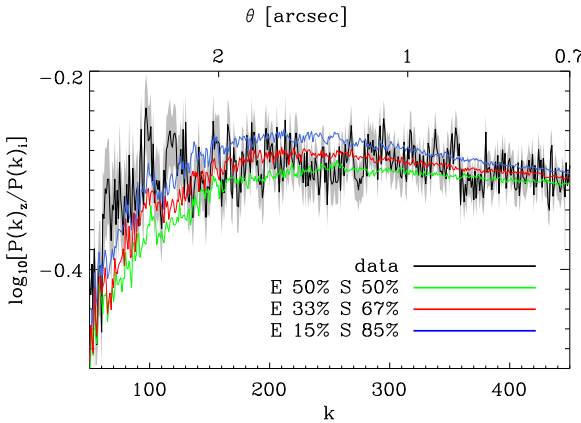


**Figure 14.** Comparison of the ratio between the  $z_{850}$  and  $i_{775}$  power spectra (black line) with the median derived from the simulations with a different percentage of spirals and ellipticals represented by different colors, 50% ellipticals and 50% spirals in green, 33% ellipticals and 67% spirals in red, and 15% ellipticals and 85% spirals in blue.

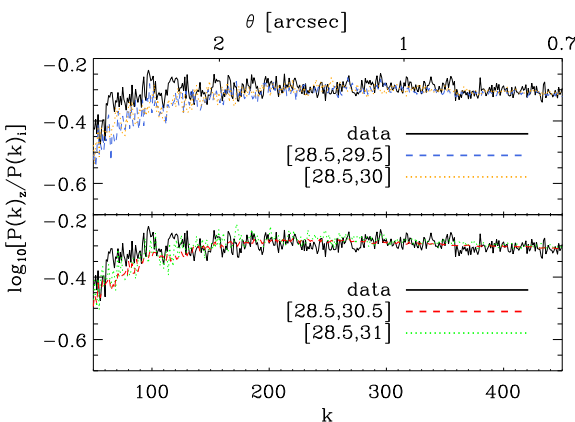


**Figure 15.** Comparison of the observed ratio between the  $z_{850}$  and  $i_{775}$  power spectra (black) and those obtained by simulating unresolved galaxies in different magnitude ranges, i.e.,  $28.5 < i_{775} < 29.5$  (blue dashed line),  $28.5 < i_{775} < 30$  (orange dotted line),  $28.5 < i_{775} < 30.5$  (red dashed line), and  $28.5 < i_{775} < 31$  (green dotted line).

galaxies (Figure 15). We used the chi-square statistics to select the best simulation concerning the magnitude cut-off (see Columns 5 and 6 in Table 3). Moreover, we computed the difference between the simulations and the data, and we plotted the residuals (Figure 16, (c) panel). On the basis of above, we decided to create galaxies with magnitudes up to 30.5 mag.

*The Mask:* Consistent results can be achieved only by analyzing the same area in data and simulations. For this reason we used, for the simulated images, the same mask created from the ACS data. Moreover, we considered what percentage of the frame is masked and calculated the number of mock galaxies that had to be outside the masked area. We, therefore, placed them randomly on the frame checking that they were positioned outside the mask.

The sum of the simulated galaxies, the frame reproducing the large scale effects, and the random noise frames was multiplied by the mask and analyzed with the power spectrum technique.

#### 4.2 Results of the Simulations

The results obtained by iterating the simulations 100 times considering the 5 bins of magnitudes given in Table 2 and assuming one third of the galaxies to be ellipticals and the others spirals are shown in Figure 17. The trend of the data with the associated errors is well fitted by the mean ratio between the simulated power spectra, and all the values are in agreement with the  $3\sigma$  confidence range.

#### 4.3 The $z \sim 6$ Faint Galaxies Contribution to Cosmic Reionization

In order to evaluate the implications for reionization of our findings, we considered the total surface brightness contribution of the undetected galaxies following the approach of Stiavelli et al. (2004a). When this contribution is added to that of detected galaxies, we find a surface brightness of  $24.8 \text{ mag arcmin}^{-2}$  when extrapolating to a magnitude  $z_{850} = 29$  mag and  $23.6 \text{ mag arcmin}^{-2}$  when extrapolating to  $z_{850} = 30$  mag. We compared these values to the minimum surface brightness of  $27.2 \text{ mag arcmin}^{-2}$  needed for reionization by Population II stars (Stiavelli et al. 2004b). Our results give comfortable margins of a factor 9 and 27, respectively, to accommodate the escape fraction  $f_c$  and the clumping factor  $C$ . For instance, assuming  $C = 6$  and the Population II spectral energy distribution (SED) of Stiavelli et al. (2004b), the LF extrapolated down to  $z_{850} = 30$  produces enough ionizing photons to reionize the Universe if  $f_c \gtrsim 5\%$ .

So far the implications for reionization of what we found seem

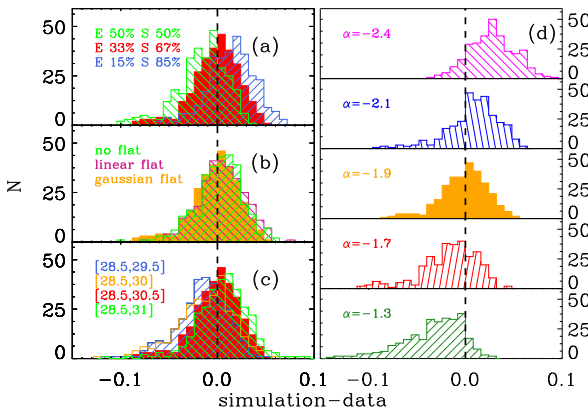


**Figure 16.** Distribution of the residuals derived computing the difference between the different realization of the simulation and the data, in terms of the ratio between power spectra in the range between  $k=100$  and  $k=400$ . The top left panel, (a), refers to the different percentages of spirals and ellipticals, the central left one, (b), to the various flat field residual models, the bottom left one, (c), concerns the magnitude cut-off, and the right one, (d), is about the different value of the faint end slope  $\alpha$ . The filled histograms refer to the selected realization, i. e. the one with the lowest  $\chi^2$ .

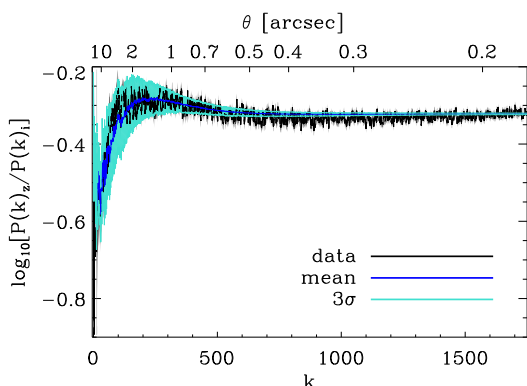


**Figure 17.** Mean ratio between the  $i_{775}$  and  $z_{850}$  simulated power spectra (blue line) and  $3\sigma$  confidence range (light blue region) derived from 100 simulations compared to the results coming from the ACS data (black line).

to be very promising, but we are waiting for a more thorough analysis of all available fields before pushing this interpretation any further.

## 5 CONCLUSIONS

In this paper we presented a new technique to quantify the light contribution coming from the faint high redshift galaxies below the detection threshold of imaging data. Specifically, we illustrated the technique with an application to ACS data obtained in the F775W and F850LP filters for the HUDF parallel field NICP12 looking for faint  $z \sim 6$  galaxies on the basis of the Lyman break technique, which is based on a comparison between the flux of a galaxy within the set of two filters.

In particular, our aim was to extend by a few magnitudes the faint end of the luminosity function at that redshift. After masking all the detected sources in the field we applied a Fast Fourier Trans-

form to obtain the spatial power spectrum of the background signal and we examined the ratio between the  $z_{850}$  and  $i_{775}$  power spectra. In this way we were able to distinguish the sources of noise from the fluctuations due to the unresolved galaxies. We tested the effect of several parameters on the power spectrum to test its reliability and how contamination can affect the results.

We showed that the power spectrum technique is a powerful tool in analyzing the light contribution produced by galaxies which are below the detection limit in deep and ultra deep surveys. We used this technique to estimate the contribution to cosmic reionization from faint galaxies ( $z_{850} \geq 28$  mag), which are bona fide  $z \sim 6$  candidates, in the NICP12 ACS field of the UDF05.

Monte Carlo simulations were used to determine the number of faint undetected  $i$ -dropouts responsible for the peak observed in the ratio between the  $z_{850}$  and  $i_{775}$  power spectra (Figure 2). The data are consistent with a faint end slope of the luminosity function of  $\alpha = -1.9$  if not introducing any clustering/grouping in the  $i_{775}$ -dropouts distribution, and  $\alpha = -1.8$  when considering pairs of galaxies with distances drawn accordingly to the angular correlation function by Lee et al. (2006). Both the  $\alpha$  values we obtained are consistent with previous findings by Yan & Windhorst (2004), Malhotra et al. (2005), Bouwens et al. (2006), Bouwens et al. (2007), Bouwens et al. (2011), and Su et al. (2011).

Considering  $\alpha = -1.9$ , adding the total surface brightness contribution of faint galaxies to that from the detected galaxies and comparing it to the minimum value required to reionize the Universe, we obtained a margin to model the escape fraction and the clumping factor. Adopting the clumping factor of 6 and Population II SED of Stiavelli et al. (2004b), the  $z \sim 6$  undetected galaxies down to  $z_{850} = 30$  mag produce enough ionizing photons to reionize the Universe assuming the escape fraction to be larger than  $\sim 5\%$ . The solution with all galaxies in pairs and a slope  $\alpha = -1.8$  changes the cumulative surface brightness by less than 0.1 mag and implies an escape fraction larger by  $\sim 10\%$ . Thus, the main conclusion of the paper that reionization is indeed consistent with being completed due to the contribution of faint galaxies is not affected by the presence of multiple halo occupation.

We expect to apply our technique to the ultra deep data obtained with NICMOS and the Wide Field Camera 3 (WFC3). The comparison of the results for different fields and instruments will permit us to better constrain the role that faint galaxies at  $z \sim 6$ ,  $z \sim 7$ , and  $z \sim 8$  had in the cosmic reionization.

## ACKNOWLEDGMENTS

We acknowledge useful conversations with Mattia Negrello and Nelson Padilla. We thank the anonymous referee for his/her comments that helped to improve our paper. This paper was supported by Padua University through grants CPDA089220/08 and CPDR095001/09, by Italian Space Agency through grant ASI-INAF I/009/10/0, by HST go grant O1374, and the JWST ids grant NAG5-12458. VC is grateful to Space Telescope Science Institute for its hospitality while part of this paper was being written. LM is supported by the University of Padua through grant No. CPS0204.

## REFERENCES

Beckwith, S. V. W., et al. 2006, AJ, 132, 1729  
 Bennett, C. L., Hill, R. S., Hinshaw, G., et al. 2003, ApJS, 148, 97

Bertin, E., & Arnouts, S. 1996, A&AS, 117, 393

Bolton, J. S., & Haehnelt, M. G. 2007, MNRAS, 382, 325

Bouwens, R. J., et al. 2004, ApJ, 616, L79

Bouwens, R. J., Illingworth, G. D., Blakeslee, J. P., & Franx, M. 2006, ApJ, 653, 53

Bouwens, R. J., Illingworth, G. D., Franx, M., & Ford, H. 2007, ApJ, 670, 928

Bouwens, R. J., Illingworth, G. D., Oesch, P. A., et al. 2011, ApJ, 737, 90

Bunker, A. J., Wilkins, S., Ellis, R. S., et al. 2010, MNRAS, 409, 855

Casertano, S., de Mello, D., Dickinson, M., et al. 2000, AJ, 120, 2747

Dahlen, T., Mobasher, B., Dickinson, M., et al. 2010, ApJ, 724, 425

de Marchi, G., Sirianni, M., Gilliland, R., et al. 2004, Detector Quantum Efficiency and Photometric Zero Points of the ACS, Instrum. Sci. Rep. 04-08 (Baltimore: STScI)

Fan, X., et al. 2001, AJ, 122, 2833

Fan, X., Carilli, C. L., & Keating, B. 2006, ARA&A, 44, 415

Ferguson, H. C., Dickinson, M., Giavalisco, M., et al. 2004, ApJ, 600, L107

Finkelstein, S. L., Papovich, C., Giavalisco, M., et al. 2010, ApJ, 719, 1250

Finkelstein, S. L., Papovich, C., Ryan, R. E., et al. 2012, ApJ, 758, 93

Giavalisco, M. 1998, The Hubble Deep Field, 121

Harrison, E. R. 1970, Phys. Rev. D, 1, 2726

Jarosik, N., et al. 2011, ApJS, 192, 14

Kashlinsky, A., Arendt, R. G., Mather, J., & Moseley, S. H. 2005, Nature, 438, 45

Kashlinsky, A., Arendt, R. G., Mather, J., & Moseley, S. H. 2007, ApJ, 666, L1

Koekemoer, A. M., Fruchter, A. S., Hook, R. N., Hack, W., & Hanley, C. 2002, The 2002 HST Calibration Workshop, ed. S. Arribas, A. M. Koekemoer, B. Whitmore (Baltimore: STScI), 337

Komatsu, E., Smith, K. M., Dunkley, J., et al. 2011, ApJS, 192, 18

Kuhlen, M., & Faucher-Giguère, C.-A. 2012, MNRAS, 423, 862

Lee, K.-S., Giavalisco, M., Gnedin, O. Y., et al. 2006, ApJ, 642, 63

Loeb, A., & Barkana, R. 2001, ARA&A, 39, 19

Lotz, J. M., Madau, P., Giavalisco, M., Primack, J., & Ferguson, H. C. 2006, ApJ, 636, 592

McLure, R. J., Dunlop, J. S., Cirasuolo, M., et al. 2010, MNRAS, 403, 960

Madau, P., Haardt, F., & Rees, M. J. 1999, ApJ, 514, 648

Malhotra, S., Rhoads, J. E., Pirzkal, N., et al. 2005, ApJ, 626, 666

Meiksin, A. 2005, MNRAS, 356, 596

Metcalfe, N., Shanks, T., Fong, R., & Roche, N. 1995, MNRAS, 273, 257

Oesch, P. A., et al. 2007, ApJ, 671, 1212

Oesch, P. A., et al. 2009, ApJ, 690, 1350

Overzier, R. A., Bouwens, R. J., Illingworth, G. D., & Franx, M. 2006, ApJ, 648, L5

Ravindranath, S., Giavalisco, M., Ferguson, H. C., et al. 2006, ApJ, 652, 963

Reach, W. T. 1997, Diffuse Infrared Radiation and the IRTS, 124, 33

Richard, J., Stark, D. P., Ellis, R. S., George, M. R., Egami, E., Kneib, J.-P., & Smith, G. P. 2008, ApJ, 685, 705

Shankar, F., & Mathur, S. 2007, ApJ, 660, 1051

Shapiro, P. R., & Giroux, M. L. 1987, ApJ, 321, L107

Somerville, R. S., Primack, J. R., & Faber, S. M. 2001, MNRAS, 320, 504

Steidel, C. C., & Hamilton, D. 1993, AJ, 105, 2017

Stiavelli, M., Fall, S. M., & Panagia, N. 2004a, ApJ, 600, 508

Stiavelli, M., Fall, S. M., & Panagia, N. 2004b, ApJ, 610, L1

Su, J., Stiavelli, M., Oesch, P., et al. 2011, ApJ, 738, 123

Tonry, J., & Schneider, D. P. 1988, AJ, 96, 807

Tonry, J. L., Ajhar, E. A., & Luppino, G. A. 1990, AJ, 100, 1416

Treister, E., Schawinski, K., Volonteri, M., Natarajan, P., & Gawiser, E. 2011, Nature, 474, 356

Trenti, M., & Stiavelli, M. 2009, ApJ, 694, 879

Trenti, M., Stiavelli, M., Bouwens, R. J., Oesch, P., Shull, J. M., Illingworth, G. D., Bradley, L. D., & Carollo, C. M. 2010, ApJ, 714, L202

White, M. 1994, A&A, 290, L1

Yan, H., & Windhorst, R. A. 2004, ApJ, 612, L93

Zeldovich, Y. B. 1972, MNRAS, 160, 1P